RESEARCH ARTICLES

QUANTUM OPTICS

An integrated diamond nanophotonics platform for quantum-optical networks

A. Sipahigil,[1]* R. E. Evans,[1]* D. D. Sukachev,[1,2,3]* M. J. Burek,[4] J. Borregaard,[1] M. K. Bhaskar,[1] C. T. Nguyen,[1] J. L. Pacheco,[5] H. A. Atikian,[4] C. Meuwly,[4] R. M. Camacho,[5] F. Jelezko,[6] E. Bielejec,[5] H. Park,[1,7] M. Lončar,[4] M. D. Lukin[1]†

Efficient interfaces between photons and quantum emitters form the basis for quantum networks and enable optical nonlinearities at the single-photon level. We demonstrate an integrated platform for scalable quantum nanophotonics based on silicon-vacancy (SiV) color centers coupled to diamond nanodevices. By placing SiV centers inside diamond photonic crystal cavities, we realize a quantum-optical switch controlled by a single color center. We control the switch using SiV metastable states and observe optical switching at the single-photon level. Raman transitions are used to realize a single-photon source with a tunable frequency and bandwidth in a diamond waveguide. By measuring intensity correlations of indistinguishable Raman photons emitted into a single waveguide, we observe a quantum interference effect resulting from the superradiant emission of two entangled SiV centers.

Efficient interfaces between photons and quantum emitters are central to applications in quantum science (*1*, *2*) but are challenging to implement due to weak interactions between single photons and individual quantum emitters. Despite advances in the control of microwave and optical fields using cavity and waveguide quantum electrodynamics (QED) (*3*–*9*), the realization of integrated quantum devices where multiple qubits are coupled by optical photons remains an outstanding challenge (*10*). In particular, due to their complex environments, solid-state emitters have optical transitions that generally exhibit a large inhomogeneous distribution (*10*, *11*), rapid decoherence (*7*), and substantial spectral diffusion, especially in nanostructures (*12*). Moreover, most solid-state emitters appear at random positions, making the realization of scalable devices with multiple emitters difficult (*11*, *13*).

Diamond platform for quantum nanophotonics

Our approach uses negatively charged silicon-vacancy (SiV) color centers (*14*) integrated into diamond nanophotonic devices. SiV centers in high-quality diamond crystals show nearly lifetime-broadened optical transitions with an inhomogeneous (ensemble) distribution on the order of the lifetime-broadened linewidth (*15*). These properties arise from the inversion symmetry of the SiV center, which protects the optical transitions from electric field noise in the environment (*16*, *17*).

The stable quantum emitters are integrated into one-dimensional diamond waveguides and photonic-crystal cavities with small mode volumes (V) and large quality factors (Q). These nanophotonic devices are fabricated using angled reactive-ion etching to scalably create freestanding single-mode structures starting from bulk diamond (*18*, *19*). As an example, Fig. 1C and fig. S3 show structures consisting of a notch for free space-waveguide coupling (at ~1% efficiency), a waveguide section on each side, and a cavity (Fig. 1B). The measured cavity $Q = 7200(500)$ is limited predominantly by decay to the waveguide, so the system has high transmission on resonance. We measure the cavity mode profile and infer $V \sim 2.5(\lambda/n)^3$ using a uniform, high-density SiV ensemble (fig. S4).

To obtain optimal coupling between an individual SiV and the cavity mode, we use a focused ion beam to implant Si^+ ions at the center of the cavities, as illustrated in Fig. 1C. To form SiVs and mitigate crystal damage from fabrication and implantation, we subsequently anneal the sample at 1200°C in vacuum (*17*). This targeted implantation technique enables positioning of emitters inside the cavity with close to 40-nm precision in all three dimensions (*19*) and control over the isotope and average number of implanted Si^+ ions. We fabricate ~2000 SiV-cavity nodes on a single diamond sample with optimal spatial alignment. For example, Fig. 1D shows fluorescence from the array of cavities implanted with Si^+ ions in Fig. 1C. SiV fluorescence is detected at

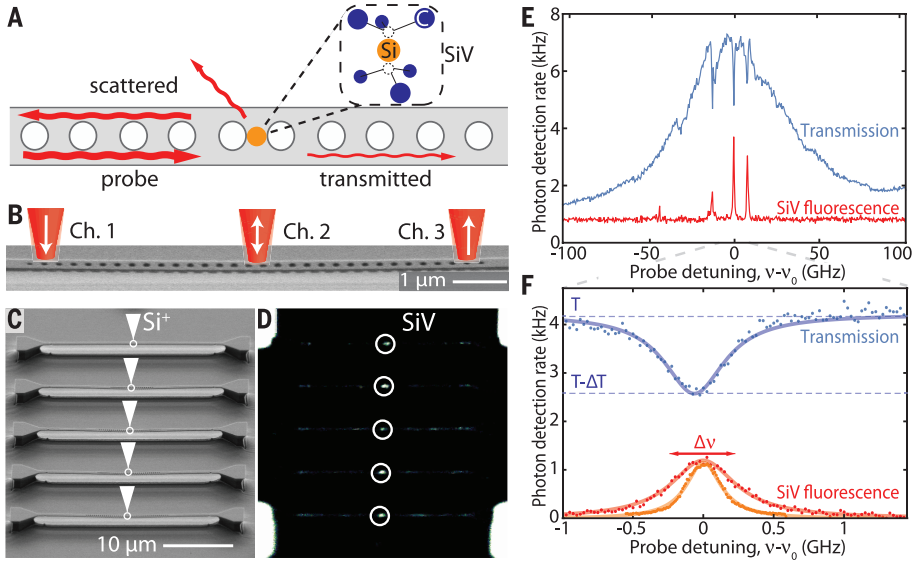

Fig. 1. Positioning and strong coupling of SiVs in diamond cavities. (**A**) Schematic of a SiV center in a diamond photonic crystal cavity. (**B**) Scanning electron micrograph (SEM) of a cavity. (**C**) SEM of five cavities fabricated out of undoped diamond. After fabrication, SiV centers are deterministically positioned at the center of each cavity using focused Si^+ ion beam implantation. (**D**) SiV fluorescence is detected at the center of each nanocavity shown in (C). (**E**) Measured cavity transmission (blue, Ch. 3) and SiV scattered fluorescence (red, Ch. 2) spectrum. Three SiV centers are coupled to the cavity, and each results in suppressed transmission. (**F**) Strong extinction, $\Delta T/T = 38(3)\%$, of probe transmission from a single SiV center. Optical transition linewidths $\Delta\nu$ are measured with the cavity detuned (orange) and on resonance (red, count rate offset by −150 Hz and multiplied by 3.3) with the SiV transition.

[1]Department of Physics, Harvard University, Cambridge, MA 02138, USA. [2]Russian Quantum Center, Skolkovo, Moscow 143025, Russia. [3]P. N. Lebedev Physical Institute of the Russian Academy of Sciences, Moscow 119991, Russia. [4]John A. Paulson School of Engineering and Applied Sciences, Harvard University, Cambridge, MA 02138, USA. [5]Sandia National Laboratories, Albuquerque, NM 87185, USA. [6]Institute for Quantum Optics, University of Ulm, 89081 Ulm, Germany. [7]Department of Chemistry and Chemical Biology, Harvard University, Cambridge, MA 02138, USA.
*These authors contributed equally to this work. †Corresponding author. Email: lukin@physics.harvard.edu

the center of each cavity, demonstrating high-yield creation of SiV-cavity nodes. The number of SiVs created varies based on the number of implanted ions and the ~2% conversion yield from Si^+ to SiV (*19*). For our experiments, we create an average of ~5 SiVs per cavity. Because each SiV can be resolved in the frequency domain, device creation is nearly deterministic: Most SiV-cavity nodes can be used for the experiments described below.

We characterize the coupled SiV-cavity system at 4 K (*19*). As shown in Fig. 1B and fig. S1, three optical beams are focused on the nanostructure to excite the waveguide mode (Channel 1), to detect fluorescence scattering and to control the SiV (Channel 2), and to detect transmission (Channel 3). In subsequent experiments (Figs. 4 and 5), efficient collection with a tapered optical fiber is employed. We scan the frequency v of the weak excitation laser across the SiV resonance $\nu_0 = 406.706$ THz and monitor the transmitted and scattered field intensities (Fig. 1E). We observe three fluorescence peaks in Channel 2 from three SiV centers in a single cavity (red curve in Fig. 1E) (*19*). At the same time, within the broad cavity transmission spectrum measured in Channel 3, each of these three resonances results in strong extinction of the cavity transmission, indicating that all three SiVs couple to the cavity mode.

The strength of the SiV-cavity coupling is evaluated using the data in Fig. 1F. When the cavity is off-resonant with the emitter, the SiV transition linewidth is $\Delta\nu = 298(5)$ MHz (orange curve) and the excited state lifetime is $\tau_e = 1.8(1)$ ns. This is close to the lifetime-broadening limit of 90 MHz, with additional nonradiative broadening likely due to a combination of finite temperature effects (*20*) and residual spectral diffusion (*17*). When the cavity is tuned into resonance (*19*), the transition is radiatively broadened to $\Delta\nu = 590(30)$ MHz (red curve), with a corresponding measured reduction in lifetime $\tau_e = 0.6(1)$ ns (limited by detection bandwidth). At the same time, we find that a single SiV results in 38(3)% extinction of the probe field in transmission (Fig. 1F, blue curve). Based on the radiative broadening shown in Fig. 1F, we infer a cooperativity of $C = 4g^2/\kappa\gamma = 1.0(1)$ for the SiV-cavity system with cavity QED parameters $\{g, \kappa, \gamma\}/2\pi = \{2.1, 57, 0.30\}$ GHz, where g is the single-photon Rabi frequency, κ is the cavity intensity decay rate, and γ is the SiV optical transition linewidth (*19*).

Quantum-optical switch based on a single SiV center

The coupled emitter-cavity system can be used to create strong interactions between single photons and achieve single-photon nonlinearities (*2*, *21*). To probe the nonlinear response of the SiV-cavity system, we repeat the transmission and linewidth measurements of Fig. 1F at increasing probe intensities. As expected (*21*, *22*), we find that the system saturates at a level less than a single photon per Purcell-enhanced excited-state lifetime (Fig. 3A), resulting in power broadening in fluorescence ($\Delta\nu$) and reduced extinction in transmission ($\Delta T/T$) (*19*).

We realize an all-optical switch with memory by optically controlling the metastable orbital states (*23*–*25*) of a single SiV (Fig. 2). Specifically, we use a 30-ns-long gate pulse to optically pump the SiV to an orbital state that is uncoupled ($|u\rangle$, Fig. 2A) or coupled ($|c\rangle$, Fig. 2B) to a weak probe field resonant with the cavity. The response of the system to the probe field after the gate pulse is monitored both in transmission (Fig. 2C) and fluorescence (Fig. 2D). If the gate pulse initializes the system in state $|c\rangle$ (blue curves), the transmission is reduced and the fluorescence scattering is increased. Initializing the system in state $|u\rangle$ (red curves) results in increased transmission and reduced fluorescence scattering. The observed modulation demonstrates switching of a weak probe pulse by a classical gate pulse. The switch memory time is limited by a thermal phonon relaxation process between $|c\rangle$ and $|u\rangle$ that depolarizes the system over $\tau_0 \sim 10$ ns at 4 K (*20*).

To investigate these processes at the single-photon level, we resonantly excite the SiV-cavity system with a weak coherent light and measure photon statistics of the scattered and transmitted fields. To this end, scattered and transmitted light are each split to two detectors (fig. S1), allowing us to measure normalized intensity autocorrelations for the scattered [$g^{(2)}_{SS}(\tau)$, Fig. 3B] and transmitted [$g^{(2)}_{TT}(\tau)$, Fig. 3C] fields, as well as cross-correlations between the two channels [$g^{(2)}_{ST}(\tau)$, Fig. 3D]. At short time scales determined by the excited state lifetime τ_e, we observe strong antibunching of photons scattered by the SiV [$g^{(2)}_{SS}(0) = 0.15(4)$], consistent with scattering from a single emitter. In transmission, the photons are strongly bunched, with $g^{(2)}_{TT}(0) = 1.50(5)$. This photon bunching in transmission results from the interference between the weak probe field and the antibunched resonant scattering from the SiV. The destructive interference for single photons yields preferential transmission of photon pairs and is a direct indication of nonlinear response at the single-photon level (*21*, *22*). In other words, a single photon in an optical pulse switches a second photon, and the

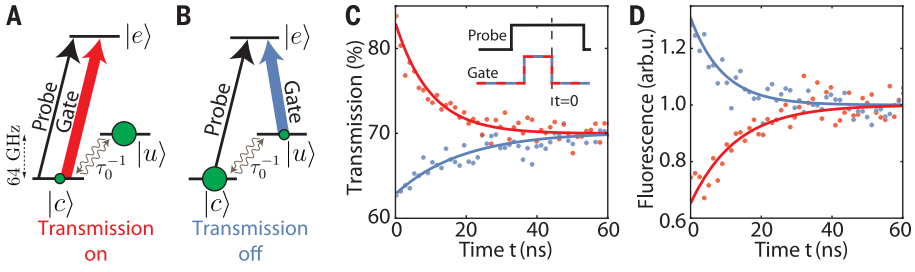

Fig. 2. An all-optical switch using a single SiV. (**A** and **B**) The transmission of a probe field is modulated using a gate pulse that optically pumps the SiV to state $|u\rangle$ (A) or $|c\rangle$ (B). (**C**) Probe field transmission measured after the initialization gate pulse. Initialization in state $|u\rangle$ ($|c\rangle$) results in increased (suppressed) transmission and (**D**) suppressed (increased) fluorescence.

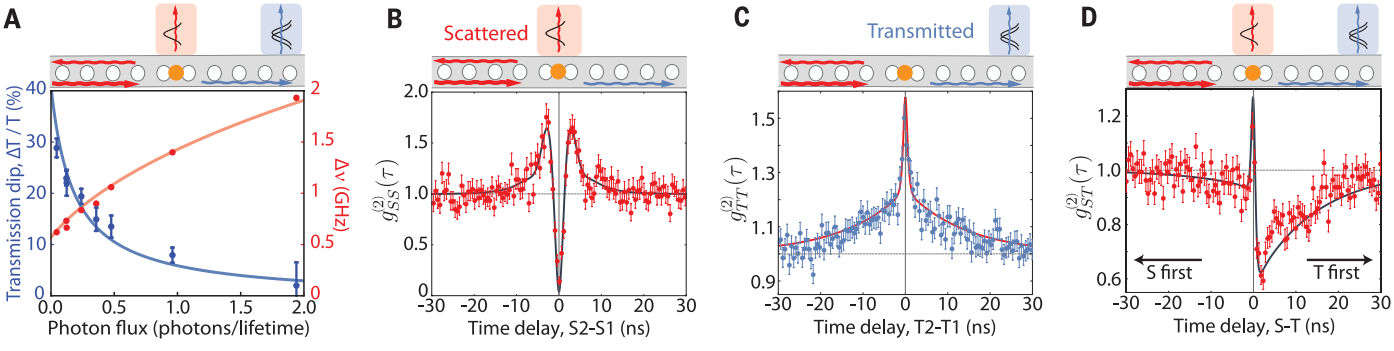

Fig. 3. Single-photon switching. (**A**) Cavity transmission and SiV transition linewidth measured at different probe intensities. (**B** and **C**) Intensity autocorrelations of the scattered (fluorescence) and transmitted fields. The scattered field shows antibunching (B), whereas the transmitted photons are bunched with an increased contribution from photon pairs (C). (**D**) Intensity cross-correlation between the scattered and transmitted fields. $g^{(2)}_{SS}$ is measured under different conditions with above-saturation excitation (*19*).

system acts as a photon number router where single photons are scattered while photon pairs are preferentially transmitted. Finally, both bunching [$g^{(2)}_{ST}(0) = 1.16(5)$] and antibunching are observed for scattering-transmission cross-correlations at fast and slow time scales, respectively.

To understand the system saturation and switching responses in Figs. 2 and 3, we model the quantum dynamics of the SiV-cavity system using the cavity QED parameters measured in Fig. 1 and a three-level model of the SiV (Fig. 2 and fig. S7). The results of our calculation (*19*) are in excellent agreement with our observations (solid curves in Figs. 1 to 3). Specifically, the presence of a second metastable state, $|u\rangle$, reduces the extinction in linear transmission (Fig. 1F) and affects the nonlinear saturation response (*19*, *21*). The metastable state $|u\rangle$ also causes both slow dynamics in photon correlation measurements (Fig. 3) at the metastable orbital relaxation timescale of τ_0 and an asymmetry in cross-correlations. In these measurements, the detection of a transmitted (scattered) photon preferentially prepares the SiV in state $|u\rangle$ ($|c\rangle$), resulting in enhanced (reduced) transmission and reduced (enhanced) scattering for τ_0 (*19*).

Tunable single-photon source using Raman transitions

A key challenge for building scalable quantum networks using solid-state emitters is the spectral inhomogeneity of their optical transitions. Although the inhomogeneous broadening of SiVs is suppressed by inversion symmetry, SiVs inside nanostructures still display a substantial inhomogeneous distribution (seen in Fig. 1E) due to residual strain from fabrication (*17*). To mitigate this effect, we use Raman transitions between the metastable orbital states of SiV centers. When a single SiV is excited from the state $|u\rangle$ at a detuning Δ (Fig. 4B), the emission spectrum includes a spontaneous component at frequency ν_{ec} and a Raman component at frequency $\nu_{ec} - \Delta$ that is tunable by choosing Δ.

Tunable single-photon emission is experimentally realized by implanting SiVs inside a one-dimensional diamond waveguide and continuously exciting the emitters from free space (Fig. 4A). The fluorescence scattering into the diamond waveguide is coupled to a tapered single-mode fiber with ≥70% efficiency using adiabatic mode transfer (*3*, *19*, *26*). As we change the excitation frequency from near-resonance to a detuning of $\Delta = 6$ GHz, we observe a corresponding tuning of the Raman emission frequency $\nu_{ec} - \Delta$, whereas the spontaneous emission frequency remains nearly fixed at ν_{ec} up to an AC Stark shift (Fig. 4C and fig. S8).

The Raman linewidth can be controlled by both the detuning and the power of the driving laser and is ultimately limited by the ground state coherence between states $|u\rangle$ and $|c\rangle$. At large detunings and low power, we measure a subnatural Raman linewidth of less than 30 MHz (fig. S8). The nonclassical nature of the Raman emission is demonstrated via photon correlation measurements. The Raman photons from a single SiV are antibunched with $g^{(2)}_{single}(0) = 0.16(3)$ (orange curve in Fig. 5D), close to the ideal limit $g^{(2)}_{single}(0) = 0$. For the continuous excitation used here, we detect Raman photons at a rate of ~15 kHz from a single SiV. After a Raman scattering event, the SiV cannot scatter a second photon within the metastable orbital state relaxation time scale τ_0, limiting the Raman emission rate. This rate can be improved using a pulsed excitation scheme, in which the SiV is first prepared in state $|u\rangle$ via optical pumping and subsequently excited with a pulse of desired shape and duration. Unlike previous demonstrations of Raman tuning of solid-state quantum emitters (*27*, *28*), the tuning range demonstrated here is comparable to the inhomogeneous distribution of the SiV ensemble and can thus be used to tune pairs of SiV centers into resonance.

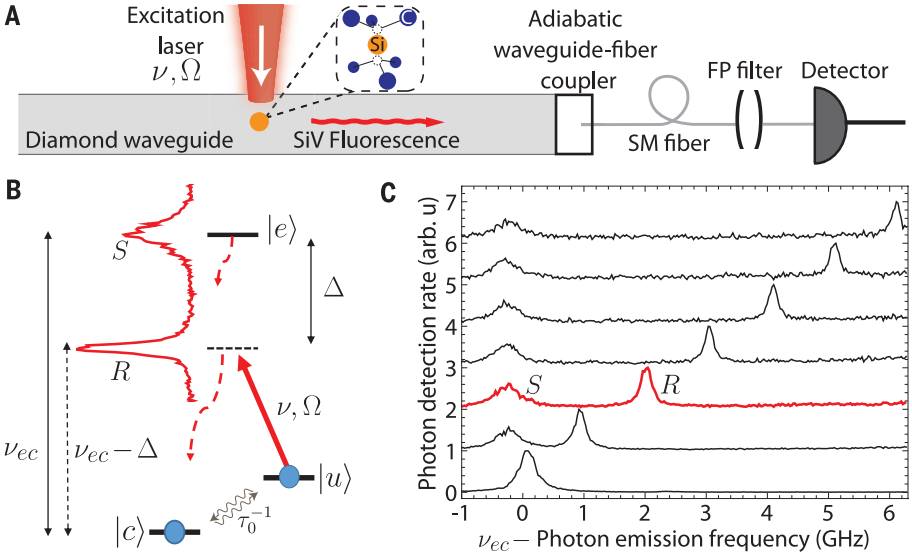

Fig. 4. Spectrally tunable single photons using Raman transitions. (**A**) Photons scattered by a single SiV into a diamond waveguide are efficiently coupled to a single-mode (SM) fiber. A scanning Fabry-Perot (FP) cavity is used to measure emission spectra (*19*). (**B**) Under excitation at a detuning Δ, the emission spectrum contains spontaneous emission (labeled *S*) at frequency ν_{ec} and narrow Raman emission (*R*) at frequency $\nu_{ec} - \Delta$. (**C**) Δ is varied from 0 to 6 GHz in steps of 1 GHz, and a corresponding tuning of the Raman emission frequency is observed. The red curves in (B) and (C) are the same data.

Entanglement of SiV centers in a nanophotonic waveguide

Quantum entanglement is an essential ingredient in quantum networks (*1*). Although optical photons were recently used to entangle solid-state qubits over long distances (*29*, *30*), optically mediated entanglement of solid-state qubits in a single nanophotonic device has not yet been observed.

Motivated by the proposals for probabilistic entanglement generation based on interference of indistinguishable photons (*31*), we use two SiV centers inside a diamond waveguide (Fig. 5A), continuously excite each SiV on the $|u\rangle \rightarrow |e\rangle$ transition with a separate laser, and measure photon correlations in the waveguide mode. If the Raman transitions of the two SiVs are not tuned into resonance, the photons are distinguishable, resulting in the measured $g^{(2)}_{dist}(0) = 0.63(3)$ (blue curve in Fig. 5D) close to the conventional limit associated with two single-photon emitters $g^{(2)}_{dist}(0) = 0.5$ (*16*, *19*). Alternatively, if the Raman transitions of the two SiVs are tuned instead into resonance with each other, an interference feature is observed in photon correlations around zero time delay, with $g^{(2)}_{ind}(0) = 0.98(5)$ (red curve in Fig. 5D).

These results can be understood by considering the level diagrams in Fig. 5, B and C, involving the SiV metastable states $|u\rangle$ and $|c\rangle$ (*8*, *32*). Photon correlation measurements probe the conditional dynamics of the two SiVs starting in state $|uu\rangle$ (*19*). In this state, each SiV scatters Raman single photons to the waveguide at a rate Γ_{1D}. However, when the Raman transitions of the two SiVs are tuned into resonance with each other, it is fundamentally impossible to distinguish which of the two emitters produced a waveguide photon. Thus, emission of an indistinguishable single photon leaves the two SiVs prepared in the entangled state $|B\rangle = (|cu\rangle + e^{i\phi}|uc\rangle)/\sqrt{2}$ (*19*, *31*) (Fig. 5B), where ϕ is set by the propagation phase between emitters spaced by ΔL and the relative phase of the driving lasers, which is constant in each experimental run (fig. S9). This state is a two-atom superradiant Dicke state with respect to the waveguide mode, independent of the value of ΔL (*19*, *32*). This implies that, although there is only a single excitation stored in the state $|B\rangle$, it will scatter Raman photons at a rate $2\Gamma_{1D}$ that is twice the scattering rate of a single emitter. This enhanced emission rate into the waveguide mode results in the experimentally observed interference peak at short time delays (Fig. 5D) and is a signature of entanglement. Our measured value of $g^{(2)}_{ind}(0) = 0.98(5)$ is close to the ideal limit, where the factor of two enhancement in the emission from the entangled state $|B\rangle$ yields $g^{(2)}_{ind}(0) = 1$.

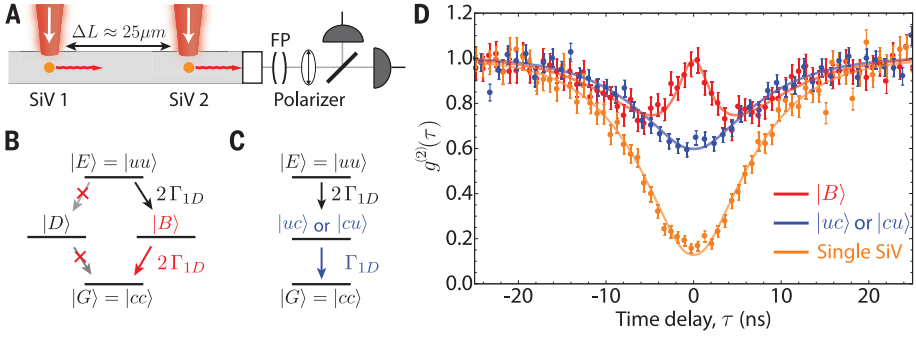

Fig. 5. Quantum interference and two-SiV entanglement in a nanophotonic waveguide. (**A**) Photons scattered by two SiV centers into a diamond waveguide are detected after a polarizer. (**B**) After emission of an indistinguishable photon, the two SiVs are in the entangled state $|B\rangle$, which decays at the collectively enhanced rate of $2\Gamma_{1D}$ into the waveguide. (**C**) After emission of a distinguishable photon, the two SiVs are in a classical mixture of states $|uc\rangle$ and $|cu\rangle$, which decays at a rate Γ_{1D} into the waveguide. (**D**) Intensity autocorrelations for the waveguide photons. Exciting only a single SiV yields $g^{(2)}_{single}(0) = 0.16(3)$ for SiV1 (orange data), and $g^{(2)}_{single}(0) = 0.16(2)$ for SiV2. Blue: Both SiVs excited; Raman photons are spectrally distinguishable. Red: Both SiVs excited; Raman photons are tuned to be indistinguishable. The observed contrast between the blue and the red curves at $g^{(2)}(0)$ is due to the collectively enhanced decay of $|B\rangle$. The solid curves are fits to a model (*19*).

The visibility of the interference signal in photon correlation measurements in Fig. 5D can be used to evaluate a lower bound on the conditional entanglement fidelity $F = \langle B|\rho|B\rangle$ (*19*). For experimental runs in which we detect a photon coincidence within the interference window (rate ~0.5 Hz), we find that the two SiVs were in an entangled state with $F \geq 82(7)\%$ after the emission of the first photon. This conditional fidelity is primarily limited by laser leakage and scattering from nearby SiVs that yield false detection events (*19*). Our measurements also demonstrate entanglement generation (rate ~30 kHz) after a single Raman photon emission event. As discussed in (*19*), using photon correlation data and steady-state populations of SiV orbital states, we find that a single photon emission results in an entangled state with positive concurrence $C > 0.090(0.024)$, which is limited by imperfect initialization in state $|uu\rangle$. The width of the interference signal in Fig. 5D can be used to extract a lifetime $T_2^* \approx 2.5$ ns of the entangled state $|B\rangle$. This lifetime is mainly limited by imperfect spectral tuning of the two Raman photons from the two SiVs, resulting in a relative frequency detuning δ. In this regime, emission of a first photon results in a state $|\psi(\tau)\rangle = (|cu\rangle + e^{i(\phi-2\pi\delta\tau)}|uc\rangle)/\sqrt{2}$ that oscillates at frequency δ between states $|B\rangle$ and the subradiant state $|D\rangle = (|cu\rangle - e^{i\phi}|uc\rangle)/\sqrt{2}$. Since $|D\rangle$ does not couple to the waveguide mode due to destructive interference, fluctuations in δ over different realizations result in decay of the collectively enhanced signal (central peak in red curve in Fig. 5D).

In our experiment, the photon propagation time is longer than T_2^* and the entangled state dephases before it can be heralded by detection of the first photon. To generate useful heralded entanglement with high fidelity (*30*, *31*), a pulsed excitation scheme can be employed in which the two SiVs are optically initialized in state $|uu\rangle$ and excited by short pulses. The Raman emission frequencies can be further stabilized using a narrowband reference cavity to extend the lifetime of the entangled state.

Outlook

The performance of these quantum nanophotonic devices can be improved in several ways. Control over the SiV orbital states is limited by the occupation of ~50 GHz phonons at 4 K, which causes relaxation between the metastable orbital states $|u\rangle$ and $|c\rangle$ and limits their coherence times to less than 50 ns. Phonon relaxation should be strongly suppressed by operating at temperatures below 300 mK or engineering the phononic density of states to enable millisecond-long coherence times (*20*). Even longer-lived quantum memories can potentially be obtained by storing the qubit in the ^{29}Si nuclear spin (*24*), which is only weakly coupled to the environment (*33*). Furthermore, the demonstrated cooperativity in our nanocavity experiment is lower than the theoretical estimate based on an ideal two-level emitter optimally positioned in a cavity (*19*). The discrepancy is due to a combination of factors, including imperfect spatial and polarization alignment, phonon broadening (*20*), finite quantum efficiency (*13*), the branching ratio of the transition, and residual spectral diffusion (*17*). These imperfections also limit the collection efficiencies obtained in our waveguide experiments. Despite uncertainties in individual contributions, operation at lower temperatures and improved cavity designs with higher Q/V ratios should enable spin-photon interfaces with high cooperativity C >> 1. Furthermore, the efficient fiber-diamond waveguide coupling can be improved to exceed 95% efficiency (*26*).

Our work demonstrates key ingredients required for realizing integrated quantum network nodes and opens up new possibilities for realizing large-scale systems involving multiple emitters strongly interacting via photons. Our fabrication approach can be used to create systems involving many coupled emitters per cavity as well as arrays of multiple atom-cavity nodes. Such a system can be used to implement entanglement generation, quantum memories, and quantum gates for either photonic or spin qubits, paving the way for the realization of scalable quantum networks (*1*, *2*).

REFERENCES AND NOTES

1. H. J. Kimble, *Nature* **453**, 1023–1030 (2008).
2. D. E. Chang, V. Vuletić, M. D. Lukin, *Nat. Photonics* **8**, 685–694 (2014).
3. T. G. Tiecke *et al.*, *Nature* **508**, 241–244 (2014).
4. A. Reiserer, N. Kalb, G. Rempe, S. Ritter, *Nature* **508**, 237–240 (2014).
5. D. Englund *et al.*, *Nature* **450**, 857–861 (2007).
6. A. Javadi *et al.*, *Nat. Commun.* **6**, 8655 (2015).
7. S. Sun, H. Kim, G. S. Solomon, E. Waks, *Nat. Nanotechnol.* **11**, 539–544 (2016).
8. J. Mlynek, A. Abdumalikov, C. Eichler, A. Wallraff, *Nat. Commun.* **5**, 5186 (2014).
9. B. Casabone *et al.*, *Phys. Rev. Lett.* **111**, 100505 (2013).
10. P. Lodahl, S. Mahmoodian, S. Stobbe, *Rev. Mod. Phys.* **87**, 347–400 (2015).
11. A. Badolato *et al.*, *Science* **308**, 1158–1161 (2005).
12. A. Faraon, C. Santori, Z. Huang, V. M. Acosta, R. G. Beausoleil, *Phys. Rev. Lett.* **109**, 033604 (2012).
13. J. Riedrich-Möller *et al.*, *Nano Lett.* **14**, 5281–5287 (2014).
14. C. Hepp *et al.*, *Phys. Rev. Lett.* **112**, 036405 (2014).
15. L. J. Rogers *et al.*, *Nat. Commun.* **5**, 4739 (2014).
16. A. Sipahigil *et al.*, *Phys. Rev. Lett.* **113**, 113602 (2014).
17. R. E. Evans, A. Sipahigil, D. D. Sukachev, A. S. Zibrov, M. D. Lukin, *Phys. Rev. Applied* **5**, 044010 (2016).
18. M. J. Burek *et al.*, *Nat. Commun.* **5**, 5718 (2014).
19. Materials and methods are available as supplementary materials on *Science* Online.
20. K. D. Jahnke *et al.*, *New J. Phys.* **17**, 043011 (2015).
21. D. E. Chang, A. S. Sørensen, E. A. Demler, M. D. Lukin, *Nat. Phys.* **3**, 807–812 (2007).
22. P. R. Rice, H. J. Carmichael, *IEEE J. Quantum Electron.* **24**, 1351–1366 (1988).
23. B. Pingault *et al.*, *Phys. Rev. Lett.* **113**, 263601 (2014).
24. L. J. Rogers *et al.*, *Phys. Rev. Lett.* **113**, 263602 (2014).
25. J. N. Becker, J. Görlitz, C. Arend, M. Markham, C. Becher, https://arxiv.org/abs/1603.00789 (2016).
26. T. G. Tiecke *et al.*, *Optica* **2**, 70–75 (2015).
27. G. Fernandez, T. Volz, R. Desbuquois, A. Badolato, A. Imamoglu, *Phys. Rev. Lett.* **103**, 087406 (2009).
28. T. M. Sweeney *et al.*, *Nat. Photonics* **8**, 442–447 (2014).
29. B. Hensen *et al.*, *Nature* **526**, 682–686 (2015).
30. A. Delteil *et al.*, *Nat. Phys.* **12**, 218–223 (2015).
31. C. Cabrillo, J. Cirac, P. Garcia-Fernandez, P. Zoller, *Phys. Rev. A* **59**, 1025–1033 (1999).
32. R. Wiegner, S. Oppel, D. Bhatti, J. von Zanthier, G. Agarwal, *Phys. Rev. A* **92**, 033832 (2015).
33. P. C. Maurer *et al.*, *Science* **336**, 1283–1286 (2012).

ACKNOWLEDGMENTS

We thank D. Twitchen and M. Markham from Element Six Inc. for substrates and K. De Greve and M. Goldman for experimental help. Financial support was provided by the NSF, the Center for Ultracold Atoms, the Air Force Office of Scientific Research Multidisciplinary University Research Initiative (MURI), the Office of Naval Research MURI, the Defense Advanced Research Projects Agency QuINESS program, the Army Research Laboratory, the Vannevar Bush Faculty Fellowship program, the Carlsberg Foundation (J.B.), and the Harvard Quantum Optics Center (M.J.B. and H.A.A.). F.J. is affiliated with the Center for Integrated Quantum Science and Technology (IQst) in Baden-Württemberg, Germany. Devices were fabricated at the Harvard Center for Nanoscale Systems supported under NSF award ECS-0335765. Ion implantation was performed with support from the Laboratory Directed Research and Development Program and the Center for Integrated Nanotechnologies at Sandia National Laboratories, an Office of Science facility operated for the DOE (contract DE-AC04-94AL85000) by Sandia Corporation, a Lockheed Martin subsidiary.

SUPPLEMENTARY MATERIALS

www.sciencemag.org/content/354/6314/847/suppl/DC1
Materials and Methods
Figs. S1 to S10
References (*34*–*40*)

1 August 2016; accepted 29 September 2016
Published online 13 October 2016
10.1126/science.aah6875

Science
AAAS

An integrated diamond nanophotonics platform for quantum-optical networks

A. Sipahigil, R. E. Evans, D. D. Sukachev, M. J. Burek, J. Borregaard, M. K. Bhaskar, C. T. Nguyen, J. L. Pacheco, H. A. Atikian, C. Meuwly, R. M. Camacho, F. Jelezko, E. Bielejec, H. Park, M. Loncar and M. D. Lukin (October 13, 2016)
Science **354** (6314), 847-850. [doi: 10.1126/science.aah6875]
originally published online October 13, 2016

Editor's Summary

Integrated quantum nanophotonics

Technologies that exploit the rules of quantum mechanics offer a potential advantage over classical devices in terms of sensitivity. Sipahigil *et al.* combined the quantum optical features of silicon-vacancy color centers with diamond-based photonic cavities to form a platform for integrated quantum nanophotonics (see the Perspective by Hanson). They could thus generate single photons from the color centers, optically switch light in the cavity by addressing the state of the color center, and quantum-mechanically entangle two color centers positioned in the cavity. The work presents a viable route to develop an integrated platform for quantum networks.

Science, this issue p. 847; see also p. 835

Science (print ISSN 0036-8075; online ISSN 1095-9203) is published weekly, except the last week in December, by the American Association for the Advancement of Science, 1200 New York Avenue NW, Washington, DC 20005.